

Quantum and Classical Chirps in an Anharmonic Oscillator

Yoni Shalibo¹, Ya'ara Rofer¹, Ido Barth¹, Lazar Friedland¹, Radoslaw Bialczack², John M. Martinis² and Nadav Katz¹

¹*Racah Institute of Physics, The Hebrew University of Jerusalem, Jerusalem 91904, Israel and*

²*Department of Physics, University of California, Santa Barbara, California 93106, USA*

We measure the state dynamics of a tunable anharmonic quantum system, the Josephson phase circuit, under the excitation of a frequency-chirped drive. At small anharmonicity, the state evolves like a wavepacket - a characteristic response in classical oscillators; in this regime we report exponentially enhanced lifetimes of highly excited states, held by the drive. At large anharmonicity, we observe sharp steps, corresponding to the excitation of discrete energy levels. The continuous transition between the two regimes is mapped by measuring the threshold of these two effects.

Ever since the laws of quantum mechanics were formulated, there has been an ongoing effort to explain the emergence of classical laws in experimental systems. The first explanation by Bohr states that these systems operate in the limit of large quantum numbers [1], in which case they may be described by a wavepacket that on the average follows the classical equations of motion [2]. In addition, coupling to uncontrolled, external degrees of freedom (decoherence), is often related to the emergence of classicality [3]. Recent experiments and calculations have demonstrated the quantum to classical transition in oscillators, via noise saturation at low temperature due to zero point fluctuations [4, 5], and harmonic behavior at high temperatures in a cavity-QED system [6].

In a classical anharmonic oscillator, such as a pendulum, the energy expectation can be deterministically increased to large values if the driving force is frequency-chirped and its amplitude is sufficiently large. This phenomenon is commonly known as autoresonance [7]. The physical mechanism behind this effect is adiabatic, nonlinear phase-locking between the system and the drive, yielding a controllable excitation as the system's resonance frequency follows the drive frequency as a function of time. This effect is utilized in a wide variety of systems [8, 9], and recently in Josephson-based oscillators [5, 10]. In a *quantum* anharmonic oscillator, the expected time evolution under a similar drive is sequential excitation of single energy levels of the system, or "quantum ladder climbing" [11]. In practice, for a given anharmonicity the drive itself introduces some mixing between the energy levels due to power broadening and finite bandwidth, which may wash out ladder climbing and lead to a classical behavior in a quantum system [12, 13]. In this letter, we measure the *dynamics* in these two distinct regimes in the same system by varying the drive parameters and the system's anharmonicity.

Our system, the Josephson phase circuit (JPC, see Fig. 1a), is a superconducting oscillator with a nonlinear inductor formed by a Josephson junction. It can be described energetically by a double-well potential that depends on the phase difference δ across the junction. We tune the potential by means of an external magnetic flux bias [14] to vary the anharmonicity and measure the

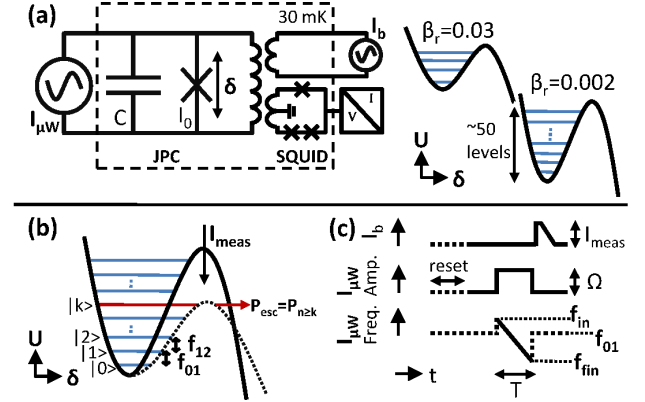


Figure 1: Operation and measurement of the Josephson phase circuit. (a) Schematics of the circuit and the potential energy at different operating biases. The potential shape and anharmonicity β_r are set by the current source I_b and the state inside the well is controlled by the microwave drive $I_{\mu W}$. (b) State measurement. A short pulse I_{meas} is applied in the flux bias to selectively tunnel excited levels $n > k$. The average phase δ is then measured with an on-chip SQUID to detect tunneling events. To determine the occupation probabilities of all the N levels, this process is repeated with a series of different I_{meas} amplitudes [18]. (c) Time sequence of the chirp experiment. The drive amplitude Ω is expressed in units of the Rabi frequency, measured on the first transition.

state. Traditionally, the circuit is operated as a two-level system (qubit) [14, 15], or a d-level system (qudit) [16], by localizing the phase δ in a shallow well where there are only a few energy levels. The quantum state of these levels is then controlled by applying nearly resonant current pulses. Due to the finite coherence time of the system, this generally requires the anharmonicity inside the well $\beta_r = (f_{01} - f_{12}) / f_{01}$ (where f_{ij} is the transition frequency from level i to level j) to be sufficiently large [17]. In this work, we vary the anharmonicity over a large range ($0.002 < \beta_r < 0.03$) in order to tune the system between the autoresonance and ladder climbing regimes. The occupation probabilities are determined by measuring the amount of tunneling out of the well due to a short pulse in the flux bias that adiabatically reduces the potential barrier (see Fig. 1b); because of the exponential dependence of the tunneling rate on the barrier height, we

get a high tunneling contrast between the states [16, 18]. Tunneling events are detected using an on-chip superconducting quantum interference device (SQUID) [19]. The experiment is repeated $\sim 10^3$ times to yield the occupation probability.

The time sequence of the experiment is sketched in Fig. 1c. Our system has negative anharmonicity ($f_{12} < f_{01}$). Therefore, we *decrease* the drive frequency at a constant rate $\alpha = 2\pi df/dt$, starting higher than the first resonance (f_{01}), in accordance with the phase locking condition. The chirp is followed by a measurement pulse in the flux bias I_{meas} and the escape probability is measured. This process is repeated for different measurement amplitudes in order to extract the state occupation probabilities P_n [18]. We start measuring the dynamics at a large anharmonicity $\beta_r = 0.023$. The time evolution is easily understood by looking at the dressed energies of the system in the rotating frame [20] (see Fig. 2a). We start the chirp in the positive detuned side ($f > f_{01}$), with the system initialized at the ground state. As the chirp progresses (decreasing detuning), it reaches an avoided-level crossing, associated with the first transition, at the frequency $f = f_{01}$. If the chirp rate α is small relative to the splitting introduced by the drive, an adiabatic transition [21] (Landau-Zener transition) to the 1st excited level occurs. As the chirp continues, the probability of staying on the adiabatic branch (ladder climbing) is higher than in the previous transition due to the increased energy splitting at higher transitions ($f = f_{i,i+1}$). Figure 2b shows the processed data of P_n vs. time along the chirp for the relevant states n . We clearly observe steps in the occupation, corresponding to the ladder climbing effect. In phase space (see insets of Fig. 2b for Wigner distribution calculated from simulation), the phase is delocalized during each step, as expected from a Fock-type state ($|\psi\rangle = |n\rangle$). In between the steps, there is a partial localization of the phase due to the interference of two such states. The fidelity of each step in the experiment (the degree of correspondence with a Fock-type state) decreases as the state number n is increased, as a result of the chirp time being comparable to the energy decay time (T_1) of the first excited state.

Next, we measure the evolution during a similar chirp but at a much smaller anharmonicity - $\beta_r = 0.002$. Lowering the anharmonicity brings about more mixing between the levels for a given drive, and may therefore result in the simultaneous excitation of many levels. Figure 2c shows the measured time evolution under these conditions. Instead of sharp steps, we notice a broad excitation during the chirp, consisting of up to 6 levels. On top of that, we observe large amplitude oscillations, as expected from autoresonant wavepacket dynamics [22]. The oscillations are also seen in phase space simulation (see inset of Fig. 2c) where the phase of the localized distribution (crescent shape) oscillates during the chirp. A detailed comparison between data and simulation, made without

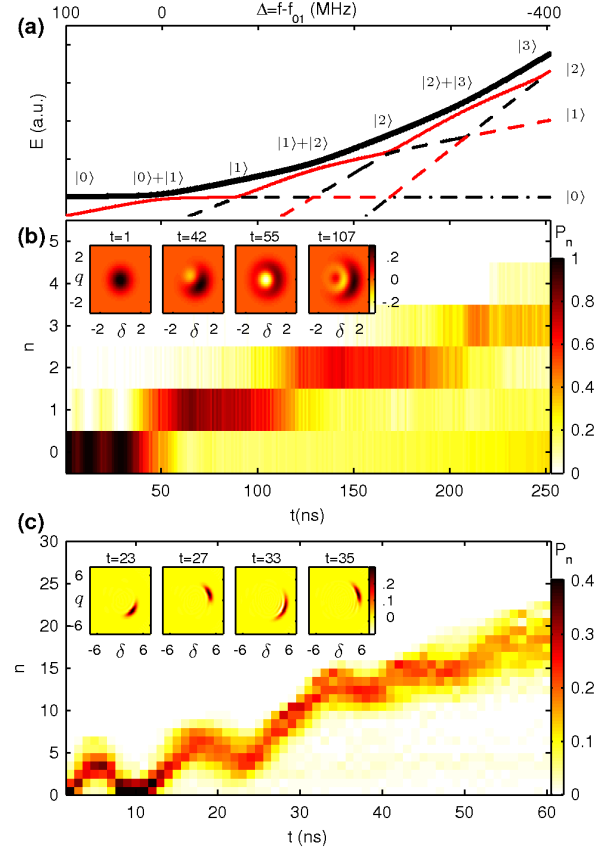


Figure 2: State dynamics during the chirp. (a) Dressed energies of the lowest levels in the rotating frame as a function of the drive frequency detuning Δ from the first transition f_{01} . As the chirp progresses (decreasing Δ), for a sufficiently small chirp rate the state remains on the adiabatic branch (solid black line). (b) Measured occupation probability (color-scale) as a function of time and level number in the ladder climbing regime ($\beta_r = 0.023$, $\alpha/2\pi = 2$ MHz/ns, $\Omega/2\pi = 27$ MHz) and (c) autoresonance regime ($\beta_r = 0.002$, $\alpha/2\pi = 10$ MHz/ns, $\Omega/2\pi = 190$ MHz). The detuning scale in (a) and the time scale in (b) are bound by the start and the end of the chirp. Insets: simulated Wigner distribution at different times along the chirp.

adjustable parameters is shown in [18].

To check the stability of the generated wavepacket at small anharmonicity, we fix the amplitude and frequency of the drive at the end of the chirp to their final value (illustrated in Fig. 3a, in the case $\Omega_{\text{hold}} = \Omega$, where Ω_{hold} is the drive amplitude after the chirp). Figure 3b shows the resulting time evolution after the chirp. The phase-locked wavepacket is centered around $n \approx 18$ and is remarkably long-lived, despite the short decay time at these highly excited levels. We define the locking probability P_{locked} as the probability to be in the phase-locked state, taken for this measurement as the integrated probability for levels $n > 10$ [13, 18]. The locking probability decays non-exponentially with a time constant $T_{\text{locked}} = 1.4 \mu\text{s}$, where T_{locked} is defined as the time it takes for the lock-

ing probability to decay to half of its initial value. The results of this experiment should be contrasted with the measurement shown in Fig. 3c, where $\Omega_{\text{hold}} = 0$. In this measurement, the energy expectation (proportional to the average level number) decays exponentially at roughly $T_1 \approx 300$ ns, consistent with the expected decay of a wavepacket in a nearly harmonic oscillator [23]. In phase space (insets of Fig. 3c) there is a quick (5 ns) delocalization into a pattern of circular fringes due to the non-negligible anharmonicity. The short lifetime-limited dephasing at $\langle n \rangle = 18$ smears out this pattern into a ring (30 ns) [24], shrinking at a constant rate $\Gamma_1 = 1/T_1$, as expected. When $\Omega_{\text{hold}} = \Omega$ (see insets of Fig. 3b), the locked population (crescent shape) remains localized, but slowly leaks out through the edge to the unlocked state, which freely decays as in Fig. 3c.

The results are explained within an effective barrier model [25, 26], where, the drive at the end of the chirp and the system's anharmonicity form an effective potential barrier for the population that is locked by the chirp. In this picture, the size of the potential barrier scales as the amplitude of the drive. We find from this theory that the resulting lifetime of the locked population is given by $T_{\text{locked}} \propto \exp(\eta\Omega_{\text{hold}}/2\pi)$ [18, 25], where the parameter η depends on the system and drive frequencies [18]. To check this model experimentally, we measure the locking probability as a function of time after the chirp and of drive amplitude. In this measurement (see Fig. 3d) the chirp parameters are fixed, but the drive amplitude at the end of the chirp is varied [27]. We find that T_{locked} scales exponentially with Ω_{hold} , supporting the effective barrier picture. The holding lifetime increases by nearly two orders of magnitude to more than $10 \mu\text{s}$. The factor η we extract from this data ($\eta \approx 26$ ns), is in agreement with theoretical prediction ($\eta \approx 30$ ns) and simulation ($\eta \approx 24$ ns) [18]. Note that in this experiment, the chirp is used to prepare the initial locked state only.

The locking probability is directly measured using a calibrated measurement pulse. In Fig. 3e, as the drive amplitude is increased near the threshold ($\Omega_{th}/2\pi \approx 30$ MHz), the highly excited (phase-locked) levels become more populated, as indicated by the increased escape probability at smaller measurement amplitudes. To measure the locking probability P_{locked} , we use a measurement amplitude that causes only the population in the upper levels to tunnel out (dashed line).

Although the state dynamics during the chirp is fundamentally different at large and small anharmonicities, it has common features in both regimes. In addition to the notable increase of the system's energy at relatively small drive amplitudes, both autoresonance and ladder climbing have a threshold in amplitude for phase-locking. While in autoresonance the threshold amplitude Ω_{th} scales as $\alpha^{3/4}$, in the ladder climbing regime $\Omega_{th} \propto \alpha^{1/2}$. The change in scaling indicates a transition between the two regimes [12]. To map the transition,

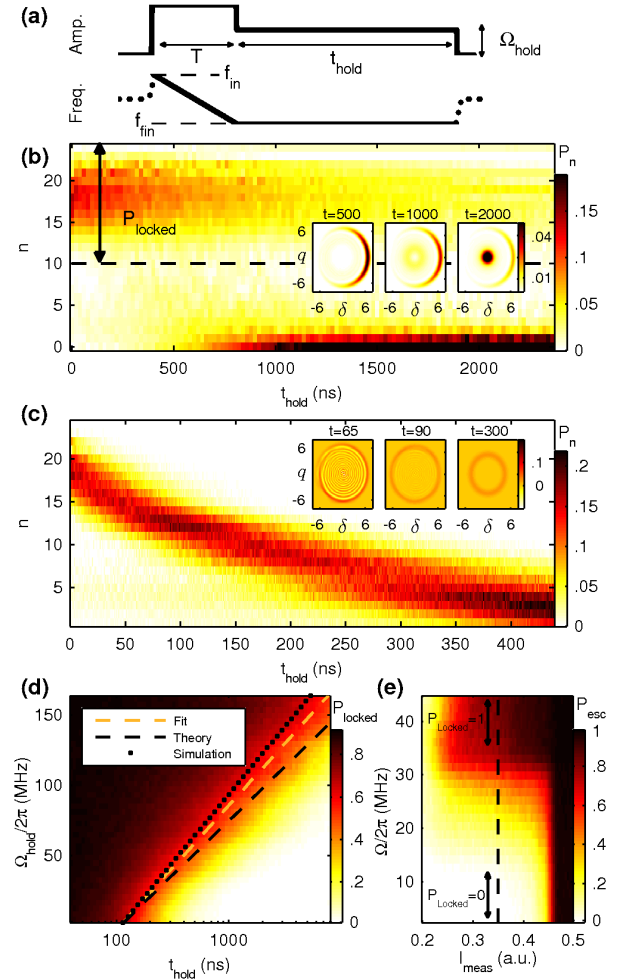


Figure 3: Decay of a wavepacket. (a) Time sequence of the decay measurement after the chirp. (b) Measured occupation probability (color-scale) as a function of level number and time after the chirp shown in Fig. 2c, with $\Omega_{\text{hold}}/2\pi = 190$ MHz and $\Omega_{\text{hold}} = 0$. Insets of (b) and (c) show the simulated Wigner plot at different times along the decay. (d) Measured locking probability (color-scale) as a function of time and amplitude of the drive after the chirp, with contours corresponding to $P_{\text{locked}}(t_{\text{hold}}, \Omega_{\text{hold}}) = 0.5$, obtained from data, theory and simulation. (e) Escape probability (color-scale) as a function of measurement amplitude I_{meas} and drive amplitude Ω after a chirp, with $\alpha/2\pi = 10$ MHz/ns and $\beta_r = 0.0046$. To measure the locking probability, an intermediate I_{meas} is used (dashed line) at the end of the chirp.

we measure the locking probability as a function of chirp rate, drive amplitude and anharmonicity.

Following Marcus et al. [12] we plot the results (see Fig. 4a) in the dimensionless parameters space, $\Omega/\sqrt{\alpha}$ and $\beta/\sqrt{\alpha}$, where $\beta = 2\pi\beta_r f_{01}$ is the absolute anharmonicity [28]. The measured threshold, defined by $P_{\text{locked}}(\Omega/\sqrt{\alpha}, \beta/\sqrt{\alpha}) = 0.5$, changes scaling (the dependence of threshold amplitude on chirp rate) at thresholds where $\beta \approx \Omega$ (blue line). This condition is met when the broadening of the first transition (caused by the drive

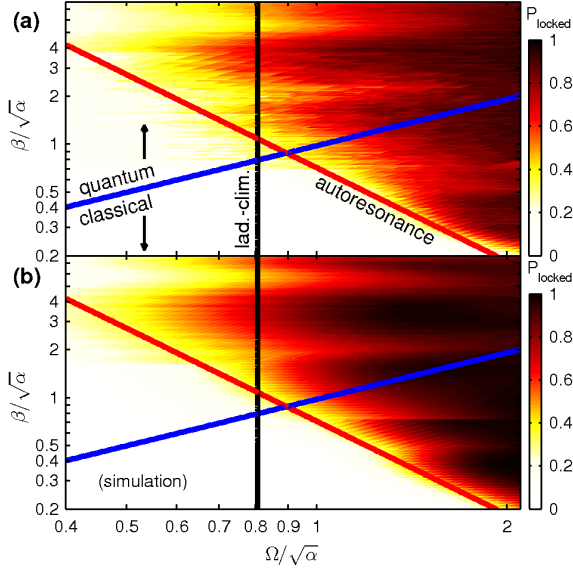


Figure 4: Transition from autoresonance to ladder-climbing. (a) Measured locking probability (color-scale) as a function of the dimensionless chirp parameters $\Omega/\sqrt{\alpha}$ and $\beta/\sqrt{\alpha}$. The red and black lines are the theoretical thresholds for autoresonance ($\Omega_{th}^{ar} = 0.82\alpha^{3/4}\beta^{-1/2}$) and ladder climbing ($\Omega_{th}^l = 0.8\alpha^{1/2}$) [13]. The blue line ($\Omega = \beta$) marks the separation between the quantum and classical regimes [12]. (b) A simulation of the experiment shown in (a) with the same parameters, including the effects of decay and measurement at different β_r [18].

amplitude) is comparable to the frequency difference between neighboring transitions. This marks the transition between the classical and quantum regimes, where the energy levels are mixed or resolved [12, 13]. For comparison, the theoretical threshold lines of autoresonance and ladder climbing are shown on the same axes in red and black respectively. Our data converges to the theoretical scaling at the classical limit. At the quantum limit the threshold shows slow oscillations as a function of $\beta/\sqrt{\alpha}$, centered on the theoretical ladder-climbing threshold line with superimposed fast oscillations [18]. The slow oscillations are reproduced by numerical simulation (see Fig. 4b) and are the result of multi-level Landau-Zener tunneling effects [13]. In the simulation, the amplitude of these oscillations decreases at larger $\beta/\sqrt{\alpha}$ values, converging to the theoretical ladder climbing threshold scaling [13].

In conclusion, the ability to measure the system's dynamics in different regimes relies on the wide-range tunability of the Josephson phase circuit. This tunability opens the possibility of measuring the full state (state tomography) of wavepackets in more coherent devices in the future. Using chirps, one can then generate and measure “cat-states” [3], within this macroscopic system. In the ladder climbing regime, one can use the chirp to generate high fidelity $|n\rangle$ states in lifetime-improved devices, without the long calibration process that is commonly re-

quired. This demonstrates the usefulness of chirped drive in creating and manipulating quantum states in the tunable Josephson phase circuit, with applications in rapid state preparation and measurement.

This work was supported by ISF grant 1248/10 and BSF grant 2008438.

-
- [1] N. Bohr, *Zeitschr. f. Physik*, **2**, 423 (1920).
 - [2] P. Ehrenfest, *Zeitschr. f. Physik A (Hadrons and Nuclei)*, **45**, 455 (1927).
 - [3] W. H. Zurek, *Rev. Mod. Phys.*, **75**, 715 (2003).
 - [4] I. Katz, A. Retzker, R. Straub, and R. Lifshitz, *Phys. Rev. Lett.*, **99**, 040404 (2007).
 - [5] K. W. Murch *et al.*, *Nat. Phys.*, **7**, 105 (2011).
 - [6] J. M. Fink *et al.*, *Phys. Rev. Lett.*, **105**, 163601 (2010).
 - [7] L. Friedland, *J. Phys. A: Math. Theor.*, **41**, 415101 (2008).
 - [8] G. B. Andresen *et al.*, *Nature*, **468**, 673 (2010).
 - [9] J. Fajans, E. Gilson, and L. Friedland, *Phys. Rev. Lett.*, **82**, 4444 (1999).
 - [10] O. Naaman, J. Aumentado, L. Friedland, J. S. Wurtele, and I. Siddiqi, *Phys. Rev. Lett.*, **101**, 117005 (2008).
 - [11] J. T. Lin, T. L. Lai, D. S. Chu, and T. F. Jiang, *J. Phys. B: At. Mol. Opt. Phys.*, **31**, L117 (1998).
 - [12] G. Marcus, L. Friedland, and A. Zigler, *Phys. Rev. A*, **69**, 013407 (2004).
 - [13] I. Barth, L. Friedland, O. Gat, and A. G. Shagalov, *Phys. Rev. A*, **84**, 013837 (2011).
 - [14] J. M. Martinis, S. Nam, J. Aumentado, and C. Urbina, *Phys. Rev. Lett.*, **89**, 117901 (2002).
 - [15] S. N. Shevchenko, A. N. Omelyanchouk, A. M. Zagorin, S. Savel'ev, and F. Nori, *New J. Phys.*, **10**, 073026 (2008).
 - [16] M. Neeley *et al.*, *Science*, **325**, 722 (2009).
 - [17] E. Lucero *et al.*, *Phys. Rev. Lett.*, **100**, 247001 (2008).
 - [18] See EPAPS document No. (?) for supplementary material.
 - [19] J. Clarke, and F. K. Wilhelm, *Nature*, **453**, 1031 (2008).
 - [20] D. F. Walls, and G. J. Milburn, *Quantum Optics*, 2nd ed. (Springer, 2007).
 - [21] C. Zener, *Proc. Roy. Soc. London A*, **137**, 696 (1932).
 - [22] J. Fajans, and L. Friedland, *Am. J. Phys.*, **69**, 1096 (2001).
 - [23] H. Wang *et al.*, *Phys. Rev. Lett.*, **101**, 240401 (2008).
 - [24] H. Wang *et al.*, *Phys. Rev. Lett.*, **103**, 200404 (2009).
 - [25] M. I. Dykman, and V. N. Smelyanskiy, *Sov. Phys. JETP*, **67**, 1769 (1988).
 - [26] M. I. Dykman, I. B. Schwartz, and M. Shapiro, *Phys. Rev. E*, **72**, 021102 (2005).
 - [27] This measurement is carried out with a different sample. The results are similar in both samples.
 - [28] The complete data set is obtained from measurements at four different anharmonicities ($\beta_r = 0.026, 0.022, 0.004, 0.002$), in order to span a large range of $\beta/\sqrt{\alpha}$ while keeping the chirp time $T = 2\pi(f_{in} - f_{fin})/\alpha$ shorter than $\sim T_1/2$, avoiding the effects of decay. We find that the threshold amplitude is affected by the decay for longer chirp times. The finite coherence time T_2 only weakly affects the threshold in our experiment [18].

Quantum and Classical Chirps in an Anharmonic Oscillator

Yoni Shalibo, Ya'ara Rofer, Ido Barth, Lazar Friedland,

Radoslaw Bialczack, John M. Martinis and Nadav Katz

Supplementary Information

Materials and methods. The Josephson phase circuit [1] used in the experiment has the following design parameters: critical current $I_0 \approx 1.5 \mu\text{A}$, capacitance $C \approx 1.3 \text{ pF}$ and inductance $L \approx 940 \text{ pH}$. The qubit has a tunable frequency f_{01} in the 6-9 GHz range [2]. During the experiment the device is thermally coupled to the mixing chamber of a dilution refrigerator at 30 mK, where thermal excitations of the qubit are negligible.

We use a custom built arbitrary waveform generator (AWG) having a fast (1 ns time resolution), 14-bit digital-to-analog converter to produce both the chirp signal and the measurement pulse. To produce the chirp, we modulate a high-frequency oscillator, having a frequency f_{LO} , using an IQ-mixer. The modulation signals, produced by the AWG, are fed into the I and Q ports of the IQ-mixer to give $\sqrt{I(t)^2 + Q(t)^2} \cos(2\pi f_{\text{LO}}t + \phi)$ at its output, where $\phi = \arctan(Q(t)/I(t))$. To produce a frequency shift from the high-frequency oscillator, we keep the amplitude at the output constant while varying the phase ϕ linearly in time; to produce a chirp, we use an accelerating phase: $\phi = 2\pi f_0 t - \alpha t^2/2$, where $f_0 = f_{\text{in}} - f_{\text{LO}}$, f_{in} is the initial frequency of the chirp, and α is the chirp rate.

To properly measure the locking probability P_{locked} , it is generally desirable to have the maximal possible chirp bandwidth $\Delta f = f_{\text{in}} - f_{\text{fin}}$ (f_{fin} being the final frequency of the chirp) in order to raise the energy expectation of the locked population higher. This leads to a better distinguishability between the locked and the unlocked population at the end of the chirp and correspondingly to an increased measurement fidelity of the locking probability, as illustrated in Fig S1. The AWG's bandwidth limitation results in an error of up to $\sim 10\%$ in P_{locked} at large anharmonicity (Fig. 1a), however it does not affect the threshold position in Fig. 4a. We use the maximal bandwidth (600 MHz), varying the modulation frequency from 300 MHz to -300 MHz [3], and setting the oscillator frequency f_{LO} 200 MHz lower than the qubit frequency f_{01} . The additional 100 MHz of bandwidth beyond the qubit frequency

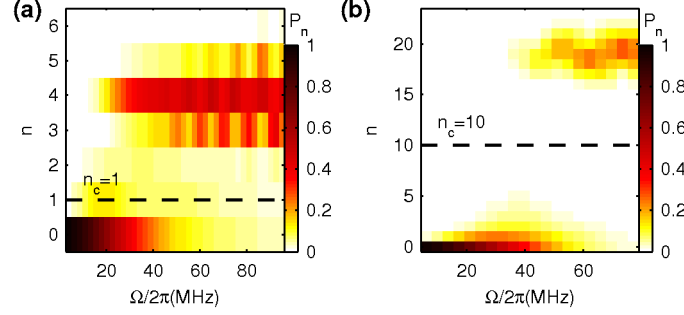


Figure S1: Level occupation of a bifurcated state after chirp in simulation, as a function of amplitude. Chirp parameters: (a) $\beta_r = 0.023$, $\alpha/2\pi = 6$ MHz/ns and (b) $\beta_r = 0.002$, $\alpha/2\pi = 12$ MHz/ns. $\Delta f = 600$ MHz and $f_{01} - f_{\text{fin}} = 500$ MHz in both. The locked and unlocked populations are discriminated by a level cutoff n_c (dashed lines), which is experimentally realized by a calibrated measurement pulse (see dashed line in Fig. 3e). At large anharmonicity relative to the chirp bandwidth (a), the locked and unlocked populations partially overlap, leading to a maximal error of $\sim 10\%$ in P_{locked} for the parameters used in the experiments.

is taken to reduce the sensitivity of the threshold to initial condition [4].

Data processing. To extract the state occupation probabilities P_n , we use the escape probabilities vs. measurement amplitude data (“escape curve”, $P_{\text{esc}}(I_{\text{meas}})$). We first measure the single-level escape curves by preparing the system in an $|n\rangle$ state, and then measuring the escape probability as a function of I_{meas} (see Fig. S2a). Once the single-level escape curves $P_{\text{esc}}^n(I_{\text{meas}})$ are at hand, we decompose the measured escape curve of an arbitrary state into the single-level basis $P_{\text{esc}}^n(I_{\text{meas}})$ by optimizing the solution P_n to the set of J equations $P_{\text{esc}}(I_{\text{meas}}^j) = \sum_n P_n P_{\text{esc}}^n(I_{\text{meas}}^j)$, where $j = 1, \dots, J$. Generating the $|n\rangle$ state becomes increasingly difficult at a larger n , due to the short lifetime of excited states. The procedure is even more problematic when the anharmonicity β is small and longer pulses are required to create the target state with reasonable fidelity. In practice, at the small anharmonicity regime that is used in the state dynamics measurement (see main paper), where $\beta/2\pi = 18$ MHz, it becomes impossible to prepare the system in an $|n\rangle$ state, even for $n > 1$. Instead, we use the first excited state escape curve, shifted by $\delta I_{\text{meas}}(n) = I_{\text{meas}}(0) - I_{\text{meas}}(n)$ as an approximate escape curve. This approximation is supported by WKB calculation (see below). To determine the position of the escape curves we use the chirp data itself: for a given state, the measured escape curve contains information about the position of the single

level escape curves. As seen in Fig. S2a, the position of these escape curves (defined as the point where the single-level escape curve increases to 0.5 of its maximal value) is determined from the positions of the peaks in the derivative $\partial P_{\text{esc}}(I_{\text{meas}})/\partial t$. Due to the finite width of the single level escape curves, the peak corresponding to a certain level is visible only when the level occupation is sufficiently large. To find $I_{\text{meas}}(n)$ for all the relevant levels, we sum the derivative over all the times along the chirp, as illustrated in Fig. S2b. The extracted $I_{\text{meas}}(n)$ values are plotted in Fig. S2c (red circles).

Simulation. To check the validity of our estimate for the escape curves, we calculate them numerically using the WKB approximation of the level dependent tunneling rates [5]:

$$\Gamma_n = f_n \exp(-2iS_n), \quad (1)$$

where $S_n = \int_{\delta_2}^{\delta_3} |p_n(\delta)| d\delta$ is the action, δ_i are the classical turning points defined in Fig. S2d, $p_n(\delta) = \sqrt{2m(E_n - U(\delta))}$ is the momentum, E_n is the energy of the n^{th} level, $U(\delta)$ is the potential energy, f_n is the classical attempt frequency, $m = C(\Phi_0/2\pi)^2$ is the effective mass and $\Phi_0 = h/2e$ is a flux quantum. f_n is calculated using the classical oscillation time: $f_n = 1/\tau$, where $\tau = \oint dt = 2 \int_{\delta_1}^{\delta_2} \frac{d\delta}{p(\delta)/m}$. The energies of the system are calculated by diagonalizing the system Hamiltonian:

$$\hat{H} = -\frac{2e^2}{C} \frac{d^2}{d\hat{\delta}^2} - \frac{I_0 \Phi_0}{2\pi} \cos \hat{\delta} + \frac{1}{2L} \left(\Phi_{\text{ext}} - \frac{\hat{\delta} \Phi_0}{2\pi} \right)^2. \quad (2)$$

The circuit parameters are found by best-fitting the calculated lowest frequencies f_{01} and f_{12} to the measured ones and fixing the number of levels in the well to 50 (the number of levels in the well is obtained from extrapolating the experimental points in Fig. S2c to $I_{\text{meas}}(P_{\text{esc}} = 0.5) = 0$) [6]. The single-level escape curves are then given by, $P_{\text{esc}}^n(I_{\text{meas}}) = 1 - \exp(-\Gamma_n(I_{\text{meas}})\Delta t)$, where Δt is the measurement pulse length. The calculated positions of the single-level escape curves are plotted in Fig. S2c (solid blue line).

We simulate the state dynamics of our N -level system under a frequency-chirped drive by propagating its density matrix ρ with the time evolution operator $U = \exp(iH_N \Delta t)$. The N -level Hamiltonian is calculated in the rotating frame of the drive, with the rotating wave approximation [7] applied:

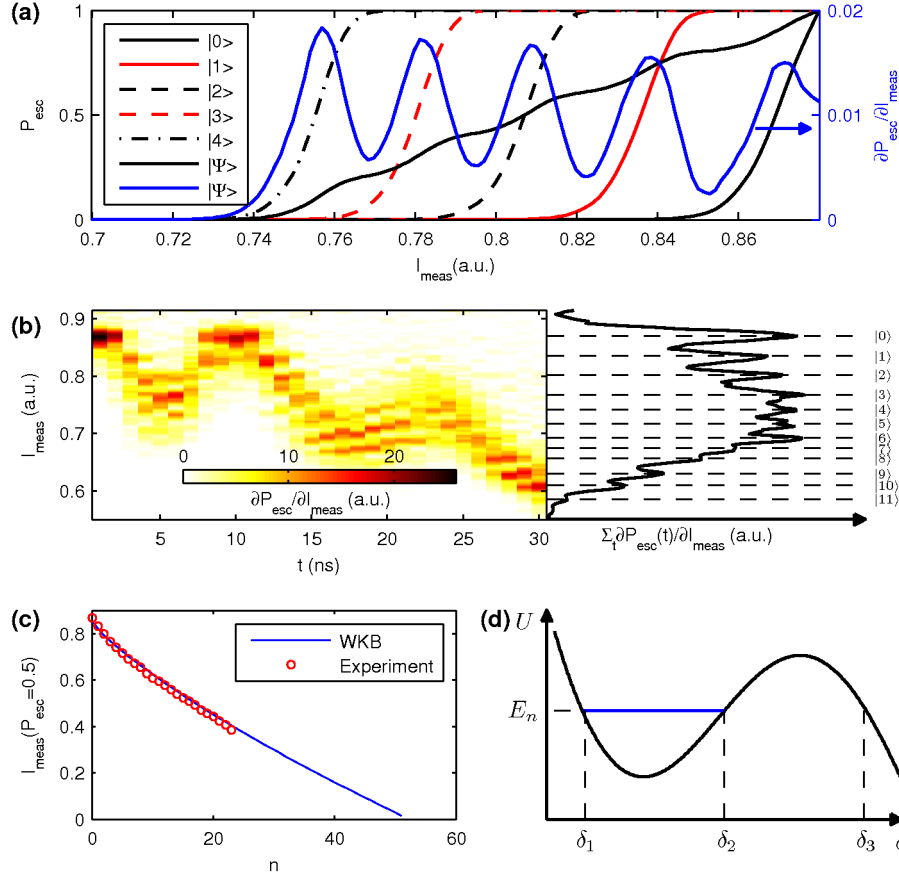


Figure S2: (a) Left axis: Calculated escape curves of single level states, and of the state $|\Psi\rangle = 1/\sqrt{5}(|0\rangle + |1\rangle + |2\rangle + |3\rangle + |4\rangle)$. Right axis: derivative of the escape curve of $|\Psi\rangle$. (b) Left panel: Derivative of the escape curve as a function measurement amplitude and time along the chirp shown in Fig. 2c. Right panel: Temporal sum of the data shown in the left panel, as a function of measurement amplitude. (c) Experimental and calculated positions of the escape curve. The WKB curve is calculated from the level dependent tunneling rates, based on the calculated energies using the best fitted circuit parameters. (d) Potential energy of the circuit used for WKB calculation, with classical turning points.

$$H_N = \hbar \begin{pmatrix} 0 & \Omega/2 & 0 & 0 & \dots & 0 \\ \Omega/2 & -\Delta & \sqrt{2}\Omega/2 & 0 & & 0 \\ 0 & \sqrt{2}\Omega/2 & \epsilon_{12} - 2\Delta & \sqrt{3}\Omega/2 & & 0 \\ 0 & 0 & \sqrt{3}\Omega/2 & \epsilon_{23} - 3\Delta & & \vdots \\ \vdots & & & & \ddots & \sqrt{N}\Omega \\ 0 & 0 & 0 & \dots & \sqrt{N}\Omega & \epsilon_{N-1,N} - (N-1)\Delta \end{pmatrix}, \quad (3)$$

where $\epsilon_{n,n+1} = 2\pi(f_{n-1,n} - f_{n,n+1})$ is the anharmonicity at the n^{th} level and $\Delta = \Delta(t) = 2\pi(f(t) - f_{01})$ is the frequency detuning of the drive and $\hbar = 2\pi\hbar$ is Planck's constant. The Rabi amplitude Ω is taken as a real constant during the chirp, and the detuning is a linearly decreasing function starting at $+2\pi \cdot 100$ MHz and ending at $-2\pi \cdot 500$ MHz, as done in the experiment. The anharmonicities $\epsilon_{n,n+1}$ are calculated from the diagonalization of the system Hamiltonian (Eq. 2). The simulation neglects deviations of matrix elements due to the drive, beyond the harmonic oscillator approximation. Namely, for $m \neq n \pm 1$, we set $\langle n | \hat{\delta} | m \rangle = 0$, and for $m = n \pm 1$ we set $\langle n | \hat{\delta} | m \rangle = \sqrt{n+1}, \sqrt{n}$. We find for the first order matrix elements ($m = n \pm 1$) a maximal deviation of order $\sim 10^{-2}$ at the largest anharmonicity, and highest states. The second order matrix elements ($m = n \pm 2$) have a maximal value of order $\sim 10^{-1}$, relative to the first order term at the same m value. Higher order elements are smaller than $\sim 10^{-4}$. For $m = n$, the contribution to the energies for the range of drive amplitudes used in the experiment is small compared with the rotating frame energies. A separate simulation taking into account all the matrix elements, without the rotating wave approximation, yields identical results in the simulations shown below (see Fig. S3b,d) to within a $\sim 10^{-2}$ deviation. Decoherence is taken into account using quantum operations [8] for amplitude and phase damping.

In Fig. S3 we plot the level populations as a function of time during the chirp shown in Fig. 2, compared with the experimental data. The simulation is calculated with no fit parameters and includes the effect of energy and phase damping. The energies at large anharmonicity (Fig. S3b) are estimated from spectroscopy data, while for small anharmonicity (Fig. S3d) they are extracted from the diagonalization of the system Hamiltonian. The experimental data and simulation agree qualitatively in both regimes. At large anharmonicity, the lengths of the “steps” are slightly different in the simulation due to the error in determining the bare transition frequencies (obtained from high power spectroscopy, where shifts and broadenings

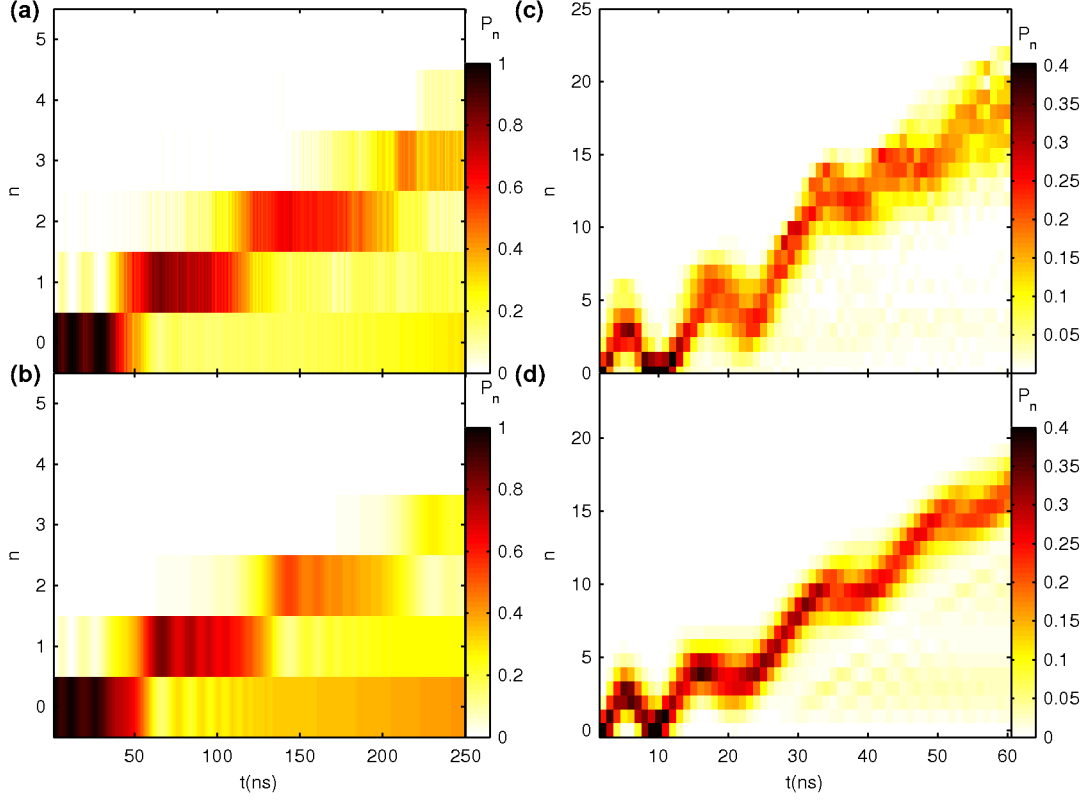


Figure S3: (a) Experimental data and (b) simulation of the dynamics experiment at large anharmonicity ($\beta/2\pi=158$ MHz) shown in Fig. 2b. (c) Experimental data and (d) simulation of the dynamics experiment at small anharmonicity ($\beta/2\pi=18$ MHz) shown in Fig. 2b.

are significant). At small anharmonicity, we see a smearing of the oscillations at higher states. This is mainly due to the frequency dependent drive amplitude. In both measurements (and simulations), we used a frequency dependent drive which decreases along the chirp as $\sqrt{n(t)}$ (where $n(t)$ is the expected average state number as a function of time) to compensate for the increasing drive coupling at higher states which increases the mixing between the levels. This, however, does not affect the locking condition which is determined from the drive amplitude at the first transition.

We compute the locking probability in the simulation by defining a cutoff n_c at intermediate levels: $P_{\text{locked}} = \sum_{n>n_c} \rho_{nn}$, where the level population vanishes (see Fig. S1). The results of this simulation are shown in Fig. 4b. All the parameters in the simulation (anharmonicities, chirp rates, drive amplitudes, and decay times) are those used/measured in the experiment.

We find that the simulation reproduces the main features of the experiment: the position of the threshold as a function of $\beta/\sqrt{\alpha}$ and consequently the transition between autoresonance and ladder climbing. The simulation (as well as the experiment), displays slow averaged features with superimposed fast oscillations. These features represent interference between adjacent levels in the driven system. We observe that the fast oscillations strongly depend on initial conditions (the distance from resonance), while the averaged slow oscillations are characteristic to the transition between the quantum and classical dynamics.

The coherence time T_2 only weakly affects the threshold in our experiment. This claim is supported by the fact that the measured threshold follows that of the decoherence free simulation despite the chirp time being longer than T_2 . In this simulation, we see that at small anharmonicity, far off-diagonal elements of the density matrix (high-order coherence terms) of a high-amplitude phase-locked wavepacket are negligible and the phase space (Wigner) representation of the wavepacket is similar to the one calculated for a classical system [9, 10]. At large anharmonicity, we find that only the first order coherences of the state ($\rho_{i,i+1}$ terms of the density matrix) are non-zero and they are significantly populated for short times (compared to the relevant dephasing time), during transitions between neighboring levels.

Theory of held drive. The locking time $T_{\text{locked}} = W^{-1}$ (where W is the decay rate from the locked state of the nonlinear resonance) is calculated by Dykman et al. in the framework of quantum activation [11]. It is shown that in the case of weak damping and at low temperatures ($k_B T \ll \hbar f_{01}$), the locking time is given by:

$$T_{\text{locked}} = c \exp(\eta \Omega / 2\pi), \quad (4)$$

where, $\eta \approx 4 / \sqrt{f_{01} |f_{\text{fin}} - f_{01}| \beta_r}$, and c is a constant on the order of T_1 . This result is valid for intermediate drive amplitudes:

$$\frac{1}{2\pi T_1} \sqrt{\frac{4 |f_{\text{fin}} - f_{01}|}{\beta_r f_{01}}} \ll \Omega / 2\pi \ll |f_{\text{fin}} - f_{01}| \sqrt{\frac{4 |f_{\text{fin}} - f_{01}|}{\beta_r f_{01}}}, \quad (5)$$

as is the case in our experiment, where these conditions translate to $4 \text{ MHz} \ll \Omega / 2\pi \ll 3.7 \text{ GHz}$.

In this theory, the dynamics are considered to be classical while the noise is quantum, and is associated with zero-point fluctuations. Moreover, the expression for the locking time coincides with the classical formula for the escape time [12], when the classical temperature

in [12] is replaced by an effective temperature, $T_{\text{eff}} = (\hbar f_{01}/2k_B) \coth(\hbar f_{01}/2k_B T)$. A more intuitive, but equivalent theory for the locking time is given by Dykman et al. [13] where the escape time from an effective potential well associated with the phase-locked state is calculated. The potential barrier in this case scales as the drive amplitude.

We find good agreement between the simulation of this experiment at several anharmonicities and the scaling predicted by Eq. 4. The theoretical prediction of the factor η , calculated using the experimental parameters (see black dashed line in Fig. 3d) is within 15 % from that obtained in the simulation with the same parameters.

-
- [1] J. M. Martinis, S. Nam, J. Aumentado, C. Urbina, Phys. Rev. Lett., **89**, 117901 (2002).
 - [2] The data in Fig. 3d is obtained from a different sample, having similar design parameters and qubit frequency range.
 - [3] We use a smaller bandwidth only in some of the measurements shown in the parameter space diagram (Fig. 4a) in order to achieve larger $\beta/\sqrt{\alpha}$ values while keeping the chirps shorter than the decay time.
 - [4] L. Friedland, J. Phys. A: Math. Theor., **41**, 415101 (2008).
 - [5] J. Ankerhold, Quantum Tunneling in Complex Systems: The Semiclassical Approach (Springer Tracts in Modern Physics) (Springer, 2007).
 - [6] The Hamiltonian in Eq. 2 is only an approximation of our system. In practice, the inductance may be flux dependent due to the small coupling between the circuit and the SQUID. For this reason, we find it difficult to obtain a good fit of the measured flux dependent energies to the calculated ones. We find that the parameters obtained from the fit have $\sim 10\%$ of uncertainty in the flux range used in the calculation.
 - [7] D. F. Walls, G. J. Milburn, Quantum Optics, 2nd ed. (Springer, 2008).
 - [8] M. A. Nielsen, I. L. Chuang, Quantum Computation and Quantum Information (Cambridge University Press, 2004).
 - [9] K. W. Murch *et al.*, Nat. Phys., **7**, 105 (2011).
 - [10] I. Barth, L. Friedland, O. Gat, A. G. Shagalov, Phys. Rev. A, **84**, 013837 (2011).
 - [11] M. I. Dykman, V. N. Smelyanskiy, Sov. Phys. JETP, **67**, 1769 (1988).
 - [12] M. I. Dykman, M. A. Krivoglaz, Sov. J. Exp. Theor. Phys., **50**, 30 (1979).

- [13] M. I. Dykman, I. B. Schwartz, M. Shapiro, Phys. Rev. E, **72**, 021102 (2005).